Textile & Leather Review

ISSN 2623-6281 | www.tlr-journal.com | 10.31881/TLR

Experimental and Numerical Investigation of the Mechanical Behavior and Stress Redistribution Mechanism in B-Doped AlCrN-Based Multilayer Coatings

Mingming Zhang, Weixuan Sun, Yingqi Sun, Hongyang Yuan, Fei Wang, Fuyang Cao

How to cite: Zhang M, Sun W, Sun Y, Yuan H, Wang F, Cao F. Experimental and Numerical Investigation of the Mechanical Behavior and Stress Redistribution Mechanism in B-Doped AlCrN-Based Multilayer Coatings. Textile & Leather Review. 2026; 9:3021-3041. https://doi.org/10.31881/TLR.2026.3021

How to link: https://doi.org/10.31881/TLR.2026.3021

Published: 25 April 2026

Experimental and Numerical Investigation of the Mechanical Behavior and Stress Redistribution Mechanism in B-Doped AlCrN-Based Multilayer Coatings

Mingming Zhang, Weixuan Sun, Yingqi Sun, Hongyang Yuan, Fei Wang*, Fuyang Cao

School of Materials Science & Engineering, Jiangsu University, Zhenjiang 212013, Jiangsu, China

*feistime@yeah.net

Article

https://doi.org/10.31881/TLR.2026.3021

Published 25 April 2026

ABSTRACT

AlCrN, AlCrBN monolayer, and AlCrBN/AlCrN multilayer coatings with various modulation periods were deposited by multi-arc ion plating. The microstructure and mechanical response of the coatings were characterized by scanning electron microscopy, X-ray diffraction, and nanoindentation, and the indentation response was further analyzed by finite element simulation. All coatings exhibited a dense structure and a single-phase face-centered cubic (fcc) phase. B addition refined the microstructure and promoted the formation of an amorphous BNx phase, whereas the multilayer design produced a clear layered architecture. Among the tested coatings, T20 showed the highest hardness (33.48 GPa), whereas T15 exhibited the highest H^3/E^{*2} value (0.116 GPa). Finite element results showed that the monolayer coatings developed a continuous semi-ellipsoidal stress field, whereas the multilayer coatings exhibited a stepwise redistribution of von Mises stress that confined the high-stress region to the upper-middle part of the coating and reduced the equivalent plastic strain. The maximum shear stress was located at a depth of about 0.6 μm below the surface. These results indicate that the local layer thickness near this depth should be considered in multilayer design to reduce the likelihood of shear-induced delamination. The study provides experimental and numerical support for the design of AlCrN-based multilayer hard coatings.

KEYWORDS

AlCrBN/AlCrN, multilayer coatings, B-doping, finite element method, stress distribution, mechanical properties

INTRODUCTION

Transition metal nitride coatings such as TiAlN- and AlCrN-based coatings are widely used on cutting tools because they improve wear resistance and service life under severe working conditions [1-4]. Among these, AlCrN coatings have attracted considerable attention due to their exceptional oxidation resistance, high

thermal stability, and robust mechanical properties [5-7]. Nevertheless, monolayer AlCrN coatings still face limitations when a high hardness level must be combined with sufficient toughness and fatigue resistance under cyclic contact conditions [8-10].

Existing literature suggests that the incorporation of Boron (B) into the AlCrN matrix facilitates the formation of a composite structure, which significantly enhances the hardness [11],wear resistance [12], and high-temperature performance [13] of CrAlBN coatings [14]. Chang et al. [15] deposited AlCrBN hard coatings via cathodic arc evaporation and observed that B addition refined the grain size from 13.7 nm (in AlCrN) to 8.7 nm, thereby promoting a denser microstructure and markedly enhancing hardness, deformation resistance, adhesion, and wear resistance. Cai et al. [16] compared AlCrBN coatings with varying B contents and reported that at 1.5 at.% B, B atoms dissolve into the fcc-(Al,Cr)N lattice to form an (Al,Cr,B)N solid solution, while concurrently forming minor amorphous $a-BN_x$ within the columnar structure, leading to enhanced hardness. Tao et al. [17] further noted that appropriate B-doping promotes grain refinement and the formation of an amorphous BN phase, thereby increasing the microhardness.

The multilayered architecture, characterized by alternating layers of different compositions or structures [18], represents another potent strategy for performance optimization [19, 20]. By periodically modulating the layer interfaces, multilayer coatings can achieve superior hardness [21], toughness [22] and fatigue resistance [23]. Coherent or semi-coherent interfaces between adjacent layers serve as effective barriers to dislocation motion and crack propagation, thus facilitating simultaneous enhancements in both hardness and toughness [24, 25]. Tritremmel et al. [26] synthesized AlTiN/AlCrBN multilayer structures and systematically analyzed their mechanical and tribological characteristics, concluding that the multilayered configuration surpassed monolayer AlCrBN in terms of hardness and wear resistance while significantly mitigating residual compressive stress. Chen et al. [27] investigated the influence of modulation geometry on TiSiN/TiAlN nanolayered coatings and found that smaller modulation periods and higher modulation ratios yielded superior high-temperature hardness and wear resistance. Chen et al. [28] demonstrated that AlCrBN/AlCrN multilayer coatings exhibited significantly higher hardness than their AlCrBN monolayer counterparts, with enhanced wear resistance.

Despite the extensive research on AlCrN-based coatings, systematic investigations into the synergistic effects of B-doping and modulation period on the microstructure, mechanical properties, and the evolution of the nanoindentation stress field in AlCrBN/AlCrN multilayer coatings remain scarce. Moreover, the mechanical response mechanisms of these multilayered structures under indentation loading warrant further elucidation.

A profound understanding of stress distribution characteristics and potential failure modes is paramount for the rational design of coating architectures and the optimization of service performance. Therefore, in this work, AlCrN, AlCrBN, and AlCrBN/AlCrN multilayer coatings with different modulation periods were prepared by multi-arc ion plating. Their microstructure and mechanical properties were characterized experimentally, and finite element simulations were used as a complementary tool to analyze the corresponding stress and strain evolution during indentation.

EXPERIMENTAL DETAILS AND MODEL DEVELOPMENT

Coating Deposition

The coatings were deposited onto cemented carbide substrates using multi-arc ion plating technology. Prior to deposition, all substrates underwent a rigorous cleaning protocol: ultrasonic cleaning in acetone for 15 minutes, followed by ultrasonic cleaning in ethanol at 65°C for an additional 15 minutes to ensure surface pristine conditions before being transferred into the vacuum chamber. The deposition was performed using a PVD system (FD, Pro 1200, China). A schematic of the equipment is depicted in Figure 1. The vacuum chamber was preheated to 480°C, followed by 15 minutes of glow discharge and 30 minutes of ion etching at a working pressure of 4 Pa. To enhance interfacial adhesion, Cr and CrN bonding layers were sequentially deposited using a pure Cr target, followed by the deposition of an AlCrN transition layer using an $Al_{70}Cr_{30}$ target with a purity of 99.95%. During the deposition of the Cr layer, CrN layer, and AlCrN transition layer, the substrate bias was maintained at −60 V, the substrate rotation speed was set to 3 rpm, and the deposition temperature was kept at 480 ℃. The deposition parameters for the Cr layer were as follows: Cr target current 120 A, Ar pressure 4.0 Pa, and deposition time 27 min. For the CrN layer, the deposition parameters were: Cr target current 120 A, N_2 partial pressure 4.0 Pa, and deposition time 55 min. For the AlCrN transition layer, the deposition parameters were: $Al_{70}Cr_{30}$ target current 120 A, N_2 partial pressure 4.0 Pa, and deposition time 60 min. After the deposition of the Cr and CrN bonding layers and the AlCrN transition layer, $Al_{70}Cr_{30}$ and $Al_{63}Cr_{27}B_{10}$ alloy targets, both with a purity of 99.95%, were used to deposit the AlCrBN/AlCrN working layers with different modulation periods. The modulation ratio of the multilayer coatings was fixed at AlCrBN:AlCrN = 1:1. By controlling the deposition sequence and deposition duration, monolayer AlCrN, monolayer AlCrBN, and multilayer coatings with 10, 15, and 20 periods were prepared. For convenience, these samples were designated as T0, T1, T10, T15, and T20, respectively. The main deposition parameters are summarized in Table 1.

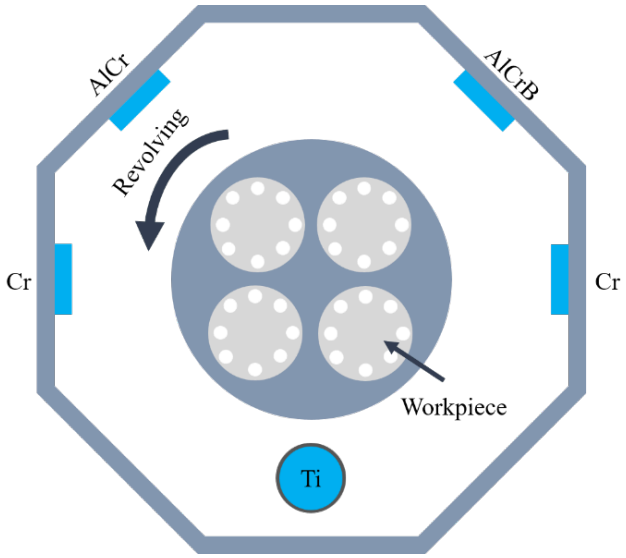

Figure 1. Schematic diagram of the deposition system

Table 1. Coating deposition parameters

Samples	Targets	Target currents (A)	Nitrogen pressure (Pa)	Monolayer Time (min)	Temperature/°C	Bias voltage/V	Rotation speed (r/min)
T0	$Al_{70}Cr_{30}$	120	4.0	180	480	−60	3
	$Al_{63}Cr_{27}B_{10}$	80		-			
T1	$Al_{70}Cr_{30}$	120	4.0	-	480	−60	3
	$Al_{63}Cr_{27}B_{10}$	80		270			
T10	$Al_{70}Cr_{30}$	120	4.0	9	480	−60	3
	$Al_{63}Cr_{27}B_{10}$	80		13.5			
T15	$Al_{70}Cr_{30}$	120	4.0	6	480	−60	3
	$Al_{63}Cr_{27}B_{10}$	80		9			
T20	$Al_{70}Cr_{30}$	120	4.0	4.5	480	−60	3
	$Al_{63}Cr_{27}B_{10}$	80		6.75			

Characterization and Testing

The cross-sectional morphology of the AlCrBN/AlCrN coatings was characterized using a field emission scanning electron microscopy (FESEM, Nova NanoSEM 450). Phase constitution was analyzed by X-ray diffraction (XRD, D8 ADVANCE) at a scanning rate of 5°/min with a step size of 0.02°over 20°–80°. Hardness and elastic modulus were measured using a nanoindenter (NHT3) operated in depth-control mode with a maximum indentation depth of 300 nm, a loading/unloading rate of 180 nm/min, and a dwell time of 10 seconds.

Because the maximum indentation depth was less than one-tenth of the coating thickness, the substrate effect on the measured hardness and elastic modulus was minimized.

Finite Element Modeling and Material Parameterization

Nanoindentation was simulated in ABAQUS to analyze the indentation-induced stress and strain fields. A two-dimensional axisymmetric model was established to reduce the computational efficiency, as shown in Figure 2. The simulation employed a depth-controlled mode. To mitigate substrate-induced artifacts in hardness calculations, the maximum indentation depth was restricted to 10% of the total coating thickness. This depth also ensures clear visualization of internal stress distribution and deformation states [29]. The indenter was modeled as a rigid equivalent of a Berkovich tip using an axisymmetric cone with a half-angle of 70.3°. While this simplification ensures an identical projected area-to-depth relationship for hardness validation, it should be noted that the axisymmetric model effectively captures the macro-scale "stress refraction" at multilayer interfaces but may underestimate localized stress concentrations occurring at the sharp edges of an actual three-sided Berkovich indenter [30]. The substrate dimensions were 17 μm × 20 μm, and the total coating thickness was 3 μm. Perfect bonding was assumed at all interfaces (substrate/AlCrN and AlCrN/AlCrBN). The bottom of the substrate was fully constrained. A refined mesh using four-node bilinear axisymmetric quadrilateral elements (CAX4) was implemented, with higher mesh density in the contact zone to ensure convergence and accuracy.

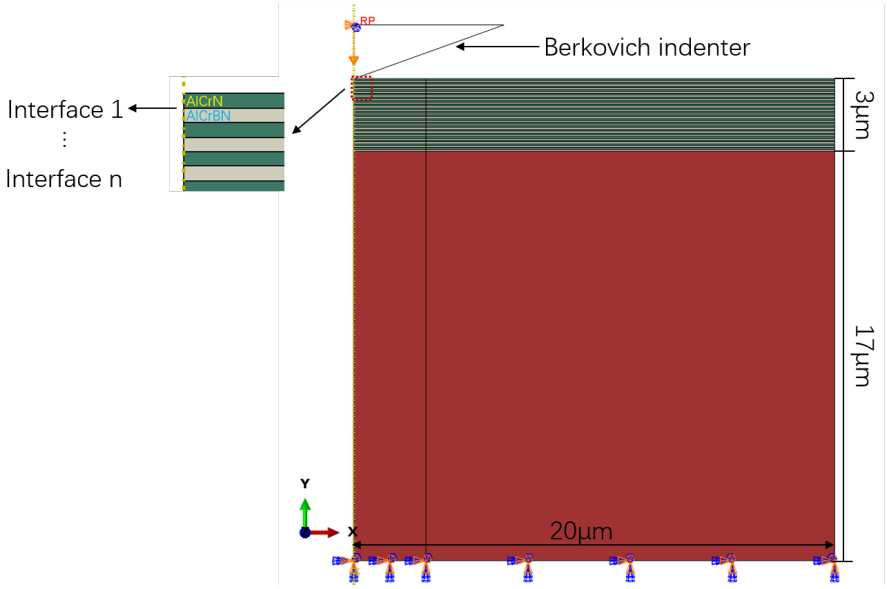

Figure 2. Finite element model

The indenter was treated as a discrete rigid body, while the substrate and coatings were modeled as elasto-plastic materials. The plastic behavior of the cemented carbide substrate was described using the Johnson-Cook (J-C) constitutive model, where the yield stress is expressed as:

$$\sigma_f = (A + B\bar{\varepsilon}_p^n)[1 + C\ln(\dot{\bar{\varepsilon}}_p/\dot{\bar{\varepsilon}}_{p0})][1 - ((T - T_r)/(T_m - T_r))^m] \quad (1)$$

In this equation, σ_f represents the equivalent yield stress, A is the initial yield strength, B is the strain hardening modulus, n is the strain hardening exponent, and C is the strain rate sensitivity coefficient. $\bar{\varepsilon}_p$ is the equivalent plastic strain, $\dot{\bar{\varepsilon}}_p$ denotes the equivalent plastic strain rate, $\dot{\bar{\varepsilon}}_{p0}$ is the reference plastic strain rate, T is the current temperature, T_r is the room temperature, T_m is the material melting point, and m is the temperature softening exponent. As the experiments were conducted at room temperature, temperature effects were neglected in the simulations. The material parameters for the indenter, substrate, and coatings are provided in Table 2. The parameters of the substrate and indenter were adopted from published literature [32, 33], whereas those of AlCrN and AlCrBN were determined experimentally in this study.

Table 2. Material parameters in the nanoindentation model

Material properties	Substrate	Diamond	AlCrN	AlCrBN
Elastic modulus (GPa)	732	1141	472	448
Poisson's ratio	0.23	0.07	0.20	0.21
A(MPa)	3001	/	12500	13800
B(MPa)	1965	/	4500	4800
n	0.2	/	0.15	0.18
C	0.03	/	/	/
$\dot{\bar{\varepsilon}}_p$	1	/	/	/

RESULTS AND DISCUSSION

Cross-sectional Morphologies

The cross-sectional microstructures of the coatings are illustrated in Figure 3. All coatings exhibit excellent interfacial integrity, with no discernible pores, cracks, or delamination at the substrate-transition layer or interlayer interfaces. This distinctly stratified architecture confirms that the transition layer effectively serves as a "buffer," accommodating the thermal expansion coefficient mismatch and enhancing overall stability [34, 35]. The interiors of all coatings are highly dense, consistent with the findings of Galindo et al. [36], who

noted that B addition suppresses columnar porosity. In Figure 3(c), the T10 coating displays an alternating dark/bright stratified structure, where the AlCrN layers appear dark and the AlCrBN layers appear bright. This contrast stems from the B-induced formation of a refined crystalline/amorphous composite in the AlCrBN layers, which produces a smoother surface and a higher secondary electron yield [37]. The thicknesses of the T0, T1, T10, T15, and T20 coatings were measured to be 2.90 μm, 2.87 μm, 2.67 μm, 2.56 μm, and 2.53 μm, respectively, which are in close agreement with the designed thicknesses during sample preparation.

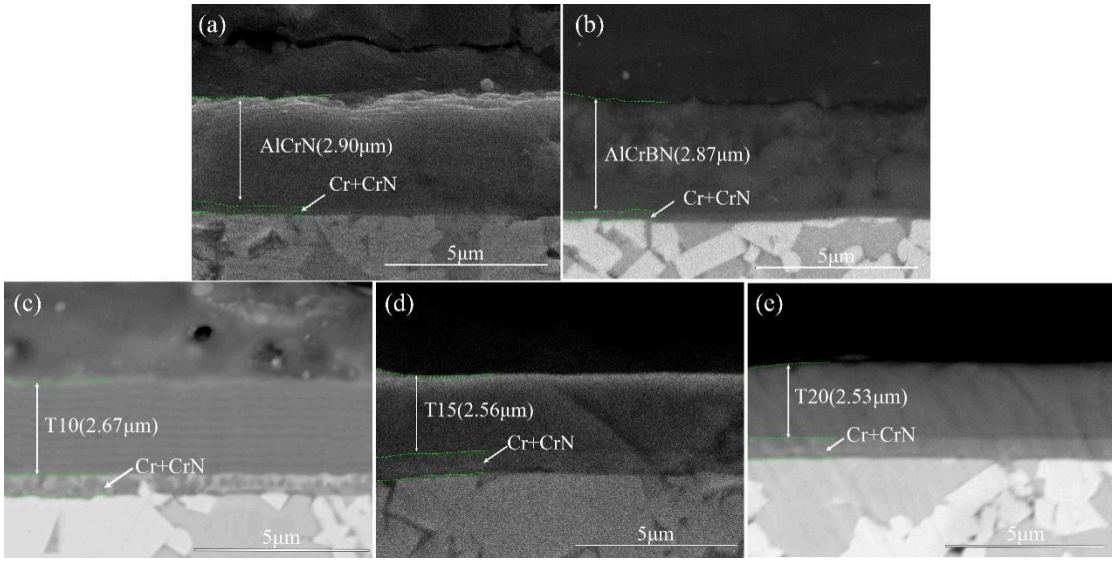

Figure 3. Cross-sectional morphology of the coatings: (a) T0; (b) T1; (c) T10; (d) T15; (e) T20

Phase Structure of the T0, T1, T10, T15 and T20 Coatings

Figure 4 displays the XRD diffraction patterns of the monolayer and multilayer AlCrBN/AlCrN coatings. Due to the excellent crystallinity of the carbide substrate, coupled with the limited thickness of the coatings, the substrate diffraction peaks exhibit exceptionally high intensity in the XRD spectra. This results in relatively weak coating diffraction signals that partially overlap with the substrate peaks. Nevertheless, the primary phase structure of the coatings can be reliably identified. All coatings present a single-phase face-centered cubic (FCC) crystalline structure [38]. The diffraction peaks corresponding to the (111), (200), (220), and (311) planes are situated between the standard positions for AlN and CrN, indicating the formation of a c-(Cr,Al)N solid solution [39]. Although B-doping did not cause significant peak shifts in XRD patterns due to the small atomic radius of B, the observed broadening of diffraction peaks suggests significant grain refinement. Based on established literature for similar B-containing systems [40], this microstructural evolution is often associ-

ated with the potential segregation of a minor amorphous BNx phase at grain boundaries, which provides a plausible explanation for the hardness enhancement despite the absence of an explicit amorphous halo in the current XRD spectra [40]. Among the multilayer coatings, the intensity of the (111) diffraction peak increases with increasing layer number, and the T20 coating shows the strongest (111) reflection, likely because the reduced sub-layer thicknesses (approx. 67.5 nm) inhibit independent nucleation and promote epitaxial growth of AlCrBN on the AlCrN template, thereby enhancing overall crystallinity [41].

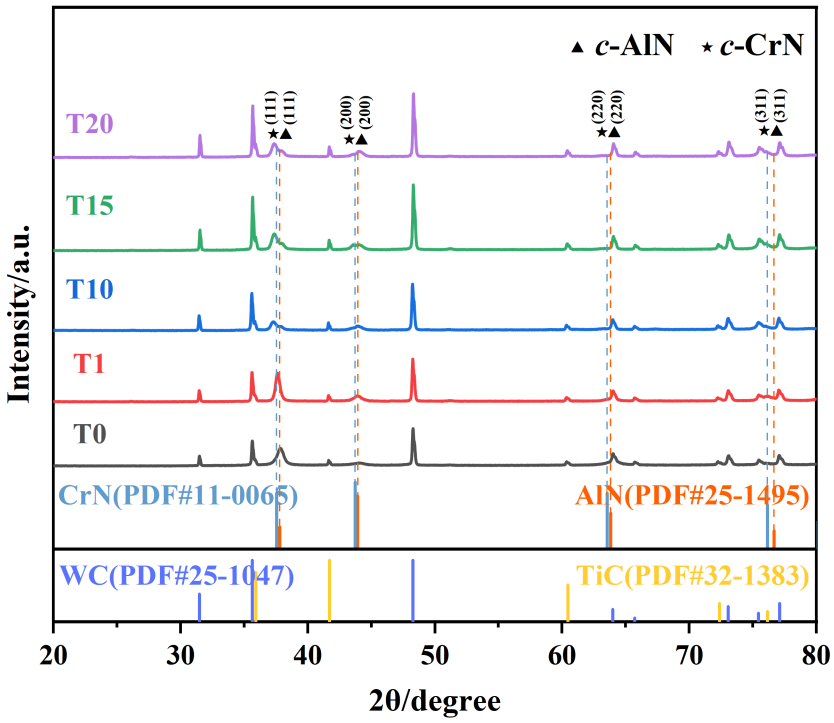

Figure 4. XRD patterns of coatings in the as-deposited state

Nanoindentation Behavior and Mechanical Properties

Figure 5 shows the load-displacement curves of the coatings. Because the tests were performed in depth-control mode, the load decreases slightly during the dwell segment while the displacement is held constant. The T0 coating shows the shallowest slope and lowest peak load, whereas B-doped and multilayered coatings (T1–T20) display significantly steeper slopes and higher peak loads, indicating enhanced resistance to plastic deformation. Multilayer coatings, particularly T15 and T20, show steeper unloading curves and reduced residual displacement, reflecting superior elastic recovery.

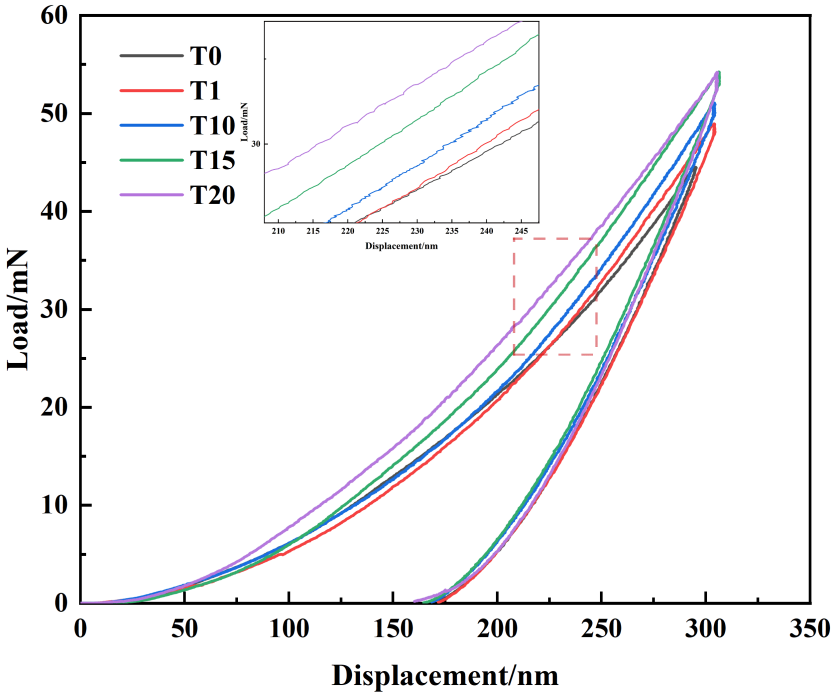

Figure 5. load-displacement curves of the coatings

Figure 6 summarizes the hardness and elastic modulus of all coatings. The T0 coating exhibited a hardness of 26.99 GPa and an elastic modulus of 472.04 GPa. Upon the introduction of boron (T1), hardness slightly increased to 29.42 GPa, while the elastic modulus decreased to 448.43 GPa. This reduction in elastic modulus is attributed to the formation of a composite structure comprising nanocrystalline AlCr(B)N and amorphous a-BN_x phases, where the amorphous phase possesses a significantly lower intrinsic elastic modulus than the nitride crystals, thus lowering the overall elastic modulus [26]. Concurrently, grain refinement and solid solution strengthening contributed to the observed increase in hardness [42]. The implementation of a multi-layer structure led to significant property enhancements. From T1 to T10, coating hardness rose from 29.42 GPa to 31.56 GPa, and elastic modulus climbed substantially from 448.43 GPa to 521.58 GPa, highlighting the interface strengthening effect. Multilayer interfaces effectively impede dislocation motion via the Hall-Petch mechanism, enhancing hardness. Moreover, optimized layer design aids in relieving internal stress and improving atomic bonding, thereby increasing elastic modulus [43]. As the number of layers increased, the hardness of the T15 coating continued to rise slowly to 32.59 GPa, but its elastic modulus decreased to 496.29 GPa. Such a divergence may be related to the higher interface density at a reduced modulation period, which enhances the influence of interfacial or transition regions on the elastic response; it is more likely associated with the increased volume fraction of interfacial regions at higher modulation periods. At

such high interface densities, the atomic structural disorder and the increased contribution of relatively compliant interfacial phases can lead to a slight reduction in the macro-elastic modulus, even while the high density of interfaces continues to effectively impede dislocation motion and enhance overall hardness via the Hall-Petch effect. However, sustained fine-grain and interface strengthening mechanisms still support a gradual increase in hardness [44]. In comparison to T15, the T20 coating showed a hardness of 33.49 GPa and a recovered elastic modulus of 538.04 GPa, indicating that this modulation period may lead to a more favorable multilayer configuration and mechanical balance. The values for effective Young's modulus (E^*), H/E, and H^3/E^{*2} are listed in Table 3. Higher H/E and H^3/E^{*2} ratios generally indicate enhanced resistance to plastic deformation and improved fracture toughness, respectively [45]. Table 3 reveals that the T15 coating possesses the highest H/E (0.066) and H^3/E^{*2} (0.116 GPa) values, suggesting superior toughness and wear resistance at room temperature.

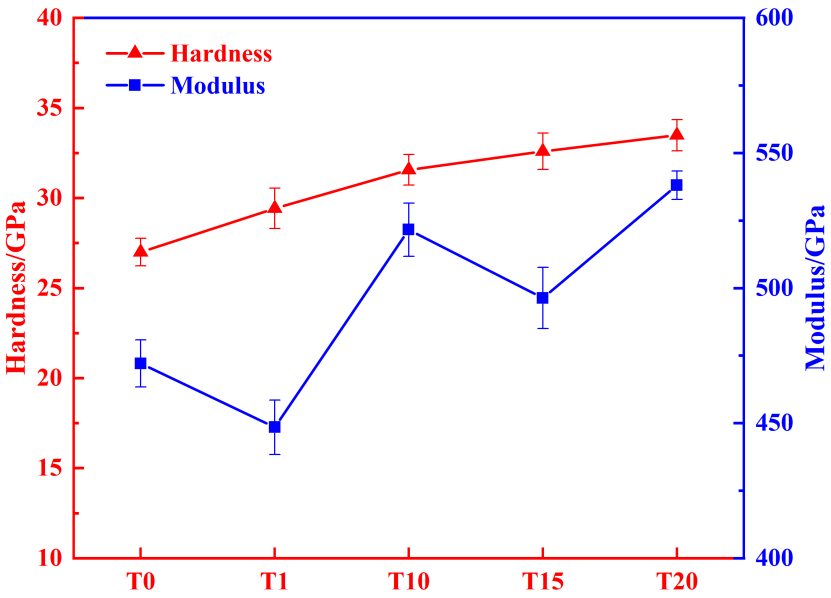

Figure 6. Micro-hardness and elastic modulus of the coatings

Table 3. Measured values of E*, H/E and H^3/E^{*2} for the coatings

Samples	E*(GPa)	H/E	H^3/E^{*2}(GPa)
T0	518.72±22.34	0.057±0.005	0.073±0.022
T1	492.78±17.41	0.065±0.007	0.105±0.008
T10	573.17±19.32	0.061±0.006	0.096±0.009
T15	545.38±10.11	0.066±0.006	0.116±0.011
T20	591.26±17.92	0.062±0.008	0.107±0.012

To further investigate the underlying mechanisms behind these experimentally observed mechanical property enhancements, a systematic finite element analysis was conducted. In the following section, we validate the numerical model using the experimental load-displacement data before examining the internal stress redistribution behaviors.

FEM Validation

The FEM model was verified by comparing the simulated and experimental P-h curves, as shown in Figure 7. For the T20 sample, the simulated peak load and residual depth are 53.05 mN and 164.92 nm, respectively, and the corresponding deviations from the experimental values are 1.1% and 4.8%. These small deviations indicate that the material parameters and model assumptions are sufficient for analyzing the relative stress and strain distributions. However, it should be noted that at an indentation depth of 300 nm, the indenter penetrates multiple sub-layers. While the simulation assumes perfect bonding, real-world multilayer structures may experience localized interfacial shear or discrete micro-cracking, which are not captured in the current continuum model. These factors likely contribute to the 4.8% deviation in residual depth, as real interfaces may provide less constraint than the ideal model suggests. The remaining discrepancy between the two curves can be attributed mainly to model simplifications, including the axisymmetric representation of the Berkovich indenter, the assumption of perfectly bonded interfaces, and the omission of local microstructural heterogeneity.

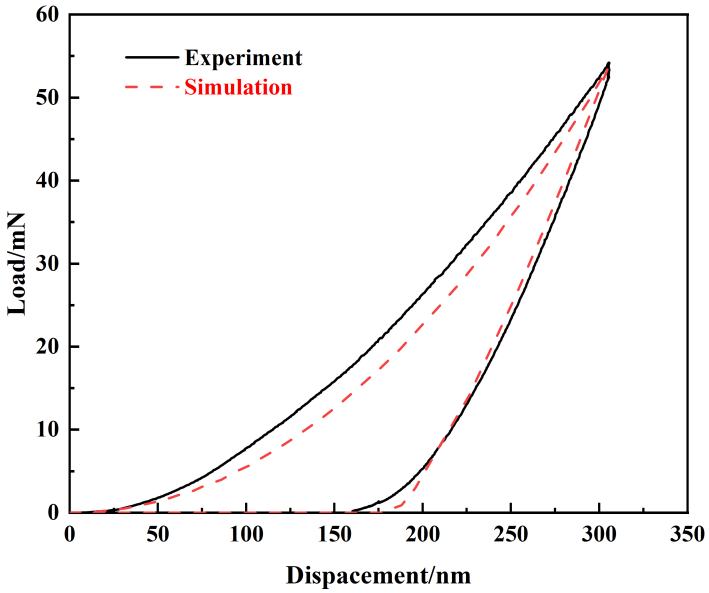

Figure 7. Comparison of simulated and experimental curves

Stress and Plastic Strain Distribution

Figure 8 shows the von Mises stress distributions of the coatings at the maximum indentation depth. For the T0 and T1 coatings, the Mises stress fields exhibit a characteristic continuous semi-ellipsoidal profile, with high-stress zones concentrated directly beneath the indenter tip and propagating along the loading axis. The peak equivalent stresses for T0 and T1 reached 21.00 GPa and 22.40 GPa, respectively. In contrast, the introduction of alternating multilayered architectures (Figure 8 c–e) alters the internal stress distribution mechanisms. In the T10, T15, and T20 coatings, the continuous stress contours are disrupted, manifesting a pronounced “staircase” decay characteristic. High-stress regions (indicated by red and orange contours) no longer penetrate continuously into the deeper layers but are effectively confined to the upper-middle regions of the coating. This phenomenon is ascribed to the elastic modulus and Poisson’s ratio mismatch between the AlCrN and AlCrBN sub-layers, which induces stress refraction and dispersion at the interfaces, thereby attenuating peak stress values and mitigating the risk of stress-concentration-induced cracking [46]. Although the maximum equivalent stresses for the multilayered coatings (22.53 GPa for T10, 22.76 GPa for T15, and 22.31 GPa for T20) are slightly higher than those of the monolayer, the stress concentration locus shifts from the surface to the coating interior, significantly lowering surface contact stress and potentially extending the service life under contact fatigue conditions.

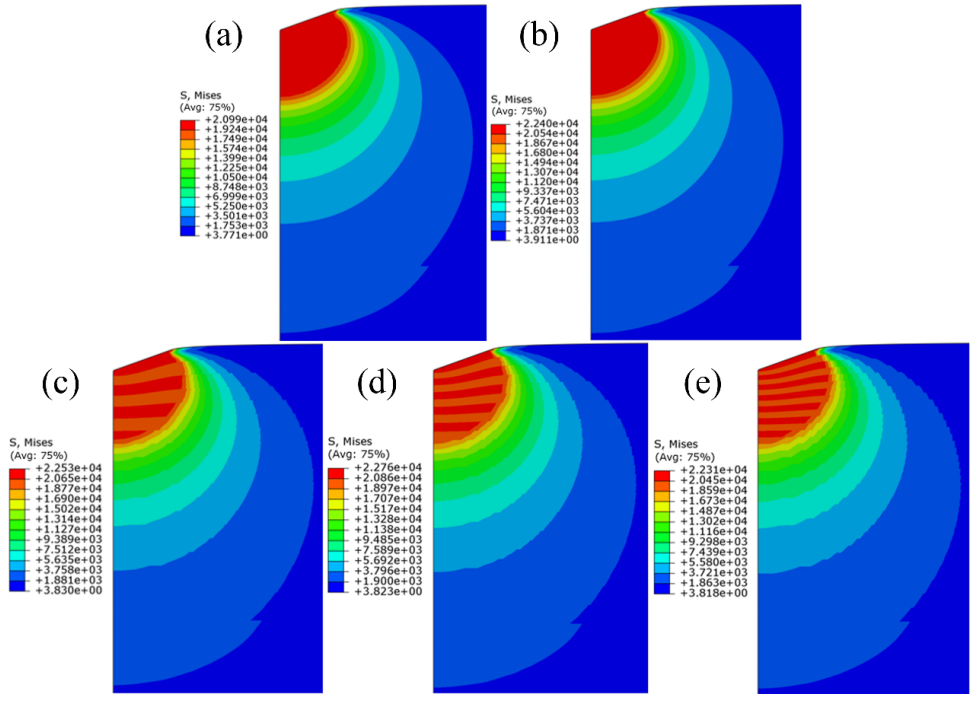

Figure 8. von Mises equivalent stress distribution contours at maximum indentation depth: (a) T0; (b) T1; (c) T10; (d) T15; (e) T20

Figure 9 presents the equivalent plastic strain (PEEQ) contours at the maximum indentation depth. For all specimens, plastic strain is predominantly localized within the contact zone beneath the indenter and the sub-surface regions, following a typical “mushroom-shaped” distribution. A comparative assessment reveals that the T0 coating exhibits the most severe plastic accumulation, with a peak PEEQ value of 1.389. The T1 coating shows a 3.24% reduction in PEEQ (1.344). This indicates that the B-containing coatings exhibit greater resistance to plastic deformation, which can be attributed to the fact that part of the incorporated B forms an interstitial solid solution and improves the yield strength via solid-solution strengthening [16]. For the AlCrN/AlCrBN multilayered coatings, the maximum PEEQ values of T10, T15, and T20 are all significantly lower than those monolayer counterparts, indicating that the multilayer architecture can effectively suppress plastic deformation during indentation. The maximum PEEQ values for the multilayer coatings T10, T15, and T20 were 1.303, 1.330, and 1.318, respectively, which are all significantly lower than their monolayer counterparts. This highlights the effectiveness of the multilayer architecture in suppressing plastic deformation. Among them, T10 exhibits the lowest maximum PEEQ, corresponding to a 6.19% reduction compared with T0. suggesting that the 10-bilayer structure provides the most favorable resistance to plastic deformation within the present parameter range. This improvement may be associated with the interfacial constraint introduced by the multilayer architecture, which promotes a more uniform distribution of plastic strain and mitigates localized strain accumulation beneath the indenter.

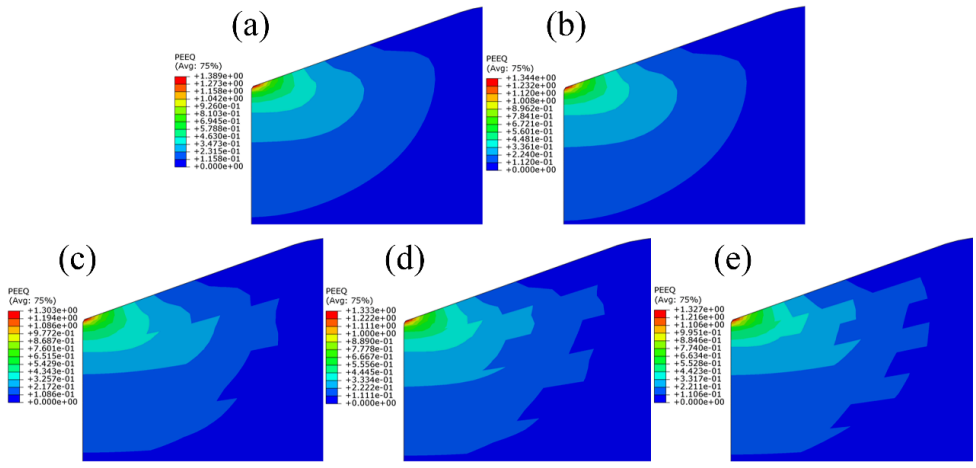

Figure 9. PEEQ equivalent plastic strain distribution contours at maximum indentation depth: (a) T0; (b) T1; (c) T10; (d) T15; (e) T20

The maximum principal stress contours (Figure 10) reveal that compressive stress levels significantly exceed tensile stress, identifying compression as the dominant mechanical response during indentation. The T0

coating exhibited a maximum tensile stress of 7.54 GPa and a maximum compressive stress of 22.7 GPa. In comparison, the T1 coating showed elevated levels of both tensile (8.11 GPa) and compressive (24.7 GPa) stresses, indicating a stronger local stress response under indentation. However, the simultaneously increased tensile stress near the coating surface may also raise the susceptibility to superficial cracking [47]. The multilayered structures (T10, T15, T20) demonstrated higher peak tensile stresses (8.67, 9.16, and 8.59 GPa, respectively) but successfully maintained or slightly reduced the peak compressive stresses (e.g., 22.1 GPa for T20). This suggests that multilayering facilitates a more balanced stress distribution by leveraging interfacial redistribution; while surface tensile levels rise slightly, sub-surface compressive concentrations are mitigated. Analysis of the layer-count effect shows that T15 reaches the highest peak tensile stress, while T20 achieves the lowest compressive stress, suggesting an optimal tuning window for modulation. This homogenized stress state is instrumental in reducing the driving force for interfacial debonding and crack initiation, thus enhancing the spallation resistance of the coatings.

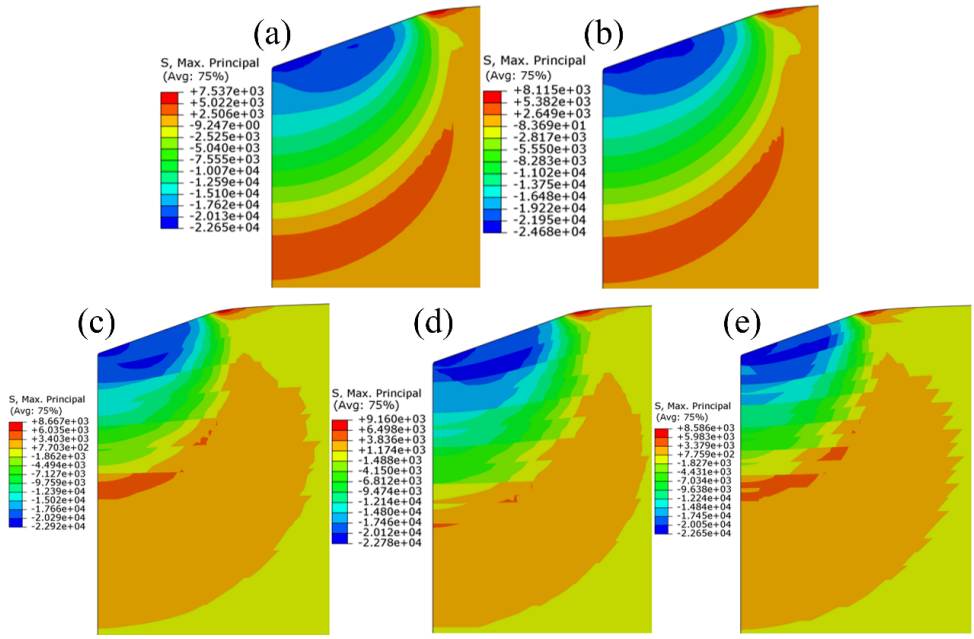

Figure 10. Max Principal stress distribution contours at maximum indentation depth: (a) T0; (b) T1; (c) T10; (d) T15; (e) T20

Figure 11 shows the shear stress component S_{12} , which represents the in-plane shear stress in the axisymmetric model. The shear stress is concentrated in the core contact zone beneath the indenter, and the high-shear region becomes smaller after the multilayer architecture is introduced. Compared with T0 and T1, the

multilayer coatings exhibit lower peak shear stress near the interface-sensitive region, indicating a reduced tendency for shear-driven damage.

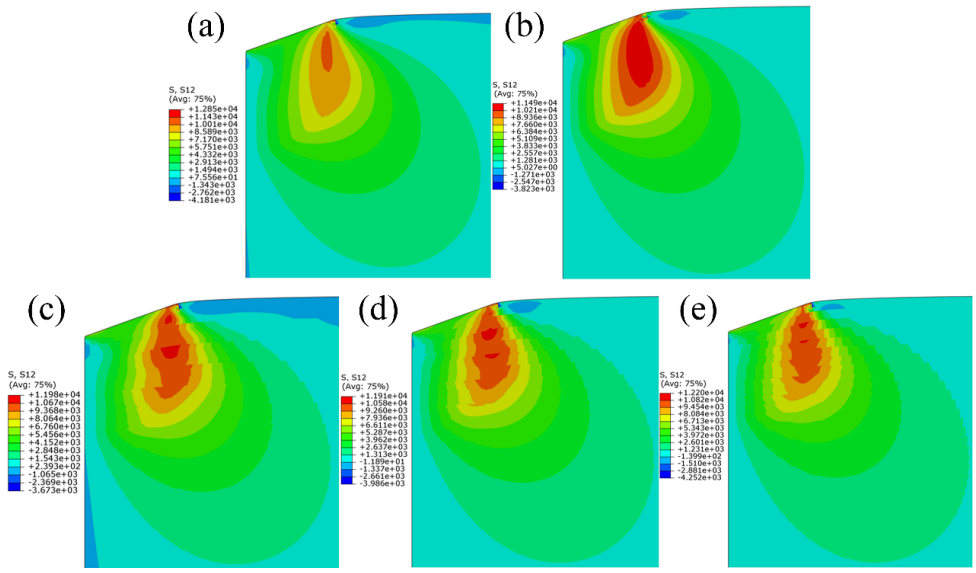

Figure 11. S12 shear stress distribution contours at maximum indentation depth: (a) T0; (b) T1; (c) T10; (d) T15; (e) T20

To further elucidate the potential failure location, shear stress values were numerically extracted from various interface positions (Figure 12). The fitted curves demonstrate that the maximum shear stress (S_{12}) remains consistently localized at a critical depth of approximately 0.6 μm, regardless of the modulation period. This stability arises because the maximum shear stress location is primarily governed by the stress bulb geometry —a function of the contact radius and the 300 nm indentation depth. In multilayered systems, while interfaces redistribute stress, the primary locus of shear loading remains fixed relative to the contact surface within this depth-control regime. However, as the interfaces migrate downward (from T10 to T20), the shear stress values at the interfaces decrease, which alleviates the shear load at the coating-substrate interface and reduces the risk of global delamination. Nevertheless, because interfaces are inherently the most compliant/weakest links in a composite system, they remain susceptible to shear-induced failure. Consequently, this study suggests a strategic structural design: by proactively increasing the thickness of the individual layer at this “perilous depth” (0.6 μm), one can ensure the maximum shear stress is confined within the bulk of a sub-layer rather than at a heterogeneous interface, thereby effectively suppressing internal shear delamination.

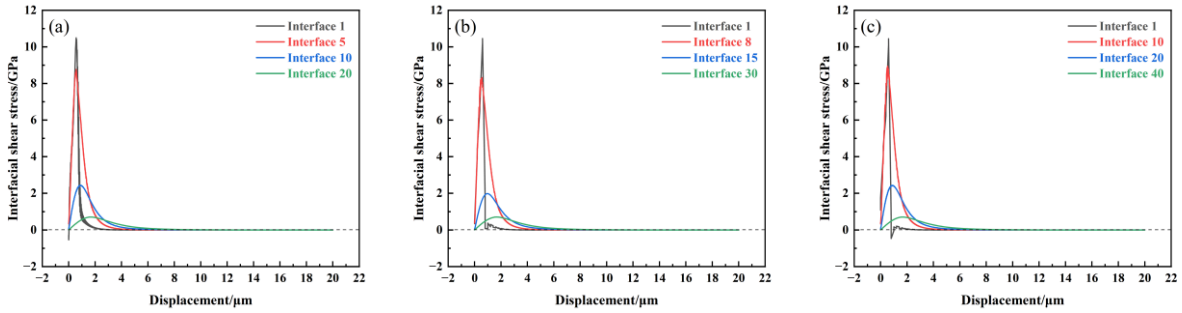

Figure 12. Shear stress distribution curves at different interface locations in multilayer coatings: (a) T10; (b) T15; (c) T20

CONCLUSIONS

The following conclusions are drawn from this systematic experimental and numerical study on B-doped AlCrN-based coatings:

(1) All coatings are dense and well-bonded to the substrate, exhibiting a single-phase fcc structure. B-doping induces grain refinement and amorphous phase formation, while the multilayered architecture facilitates localized epitaxial growth, with T20 showing the highest crystallinity.

(2) The multilayered structure enables simultaneous improvements in hardness and toughness. The T20 coating attained the maximum hardness (33.48 GPa) due to Hall-Petch interfacial strengthening. The T15 coating achieved an optimal H^3/E^{*2} value (0.116 GPa), indicating that moderate interfacial density maximizes stress relaxation and resistance to plastic deformation.

(3) FEM simulations reveal that multilayer coatings leverage modulus mismatch to transform a continuous stress field into a “staircase” decay profile. This confines high-stress regions to the upper-middle layers and significantly lowers the PEEQ, thereby enhancing contact fatigue resistance.

(4) Shear stress analysis identifies a “perilous depth” at 0.6 μm where maximum shear stress resides, regardless of modulation. To prevent internal delamination, multilayer design should prioritize increasing the thickness of the individual layer at this specific depth to avoid situating a heterogeneous interface within the high-shear zone.

Author Contributions

Conceptualization –Mingming Zhang, Weixuan Sun, Yingqi Sun, Hongyang Yuan, Fei Wang, Fei Cai and Fuyang Cao; methodology – Mingming Zhang, Weixuan Sun, Yingqi Sun, Hongyang Yuan, Fei Wang, Fei Cai and Fuyang Cao; investigation – Mingming Zhang, Weixuan Sun, Yingqi Sun, Hongyang Yuan, Fei Wang, Fei Cai and Fuyang

Cao; writing-original draft preparation – Mingming Zhang, Weixuan Sun, Yingqi Sun, Hongyang Yuan, Fei Wang, Fei Cai and Fuyang Cao. All authors have read and agreed to the published version of the manuscript.

Conflicts of Interest

The authors declare no conflict of interest.

Funding

This research received no external funding.

Acknowledgements

The authors gratefully acknowledge the support from the School of Materials Science and Engineering, Jiangsu University, and the Key Laboratory of Green Fabrication and Surface Technology of Advanced Metal Materials, Ministry of Education, Anhui University of Technology. The authors also thank all colleagues who provided assistance with coating preparation, characterization, nanoindentation testing, and finite element simulation during this work.

REFERENCES

[1] Shankar E, Sampath Kumar T, Devanathan C, Giri Sankar S, Dhandapani S, Natarajan MS. Comparative study of metallurgical and machinability characteristics of boronised and coated tungsten carbide inserts using EN19 steel as workpiece. Materials Today: Proceedings. 2021; 46:3398-3403. doi: 10.1016/j.matpr.2020.11.583

[2] Yue QB, He HB, Li HY, Zhang J, Li YM, Ma L. Research on Friction Characteristics of AlCrN and TiAlSiN Coatings and Properties of Coated Tools. International Journal of Precision Engineering and Manufacturing. 2019; 20:1581-1589. doi: 10.1007/s12541-019-00168-z

[3] He Z, Wang S, Li R, Pu J, Wang Y, Yao J. Effect of stress loading on hot salt corrosion behavior of TiAlTaN/CrAlN multilayer coatings. Corrosion Science. 2023; 220:111286. doi: 10.1016/j.corsci.2023.111286

[4] Wang D, Lin SS, Lu JD, Huang SQ, Yin ZF, Yang HZ, Bian PY, Zhang YL, Dai MJ, Zhou KS. Research on high temperature wear resistance mechanism of CrN/CrAlN multilayer coatings. Tribology International. 2023; 180:108184. doi: 10.1016/j.triboint.2022.108184

[5] Souza PS, Santos AJ, Cotrim MAP, Abrão AM, Câmara MA. Analysis of the surface energy interactions in the tribological behavior of ALCrN and TIAlN coatings. Tribology International. 2020; 146:106206. doi: 10.1016/j.triboint.2020.106206

[6] Varghese V, Akhil K, Ramesh MR, Chakradhar D. Investigation on the performance of AlCrN and AlTiN coated cemented carbide inserts during end milling of maraging steel under dry, wet and cryogenic environments. Journal of Manufacturing Processes. 2019; 43:136-144. doi: 10.1016/j.jmapro.2019.05.021

[7] Chang YY, Weng SY, Chen CH, Fu FX. High temperature oxidation and cutting performance of AlCrN, TiVN and multilayered AlCrN/TiVN hard coatings. Surface and Coatings Technology. 2017; 332:494-503. doi: 10.1016/j.surfcoat.2017.06.080

[8] Wang J, Liu Z, Wu Y, Wang Q, Shu D. Cutting Performance and Tool Wear of AlCrN- and TiAlN-Coated Carbide Tools during Milling of Tantalum-Tungsten Alloy. 2024; 12:170. doi: 10.3390/machines12030170

[9] Liu J, Mei H, Hua J, Wang J, Wang Y, Yi G, Deng XJ. High-Temperature Oxidation and Wear Resistance of TiAlSiN/AlCrN Multilayer Coatings Prepared by Multi-Arc Ion Plating. 2025; 15. doi: 10.3390/nano15070503

[10] Liu J, Wang Y, Liu G, Hua J, Deng X. Properties and Performance of TiAlSiN and AlCrN Monolayer and Multilayer Coatings for Turning Ti-6Al-4V. 2023; 13:1229. doi: 10.3390/coatings13071229

[11] Nguyen QD, Ueno S. Improvement of sensorless speed control for nonsalient type axial gap self-bearing motor using sliding mode observer. in: 2010 IEEE International Conference on Industrial Technology, 2010, pp. 373-378. doi: 10.1109/ICIT.2010.5472709

[12] Nguyen HC, Joska Z, Pokorny Z, Studeny Z, Sedlák J, Majerík J, Svoboda E, Dobrocky D, Procházka J, Tran QD. Effect of Boron and Vanadium Addition on Friction-Wear Properties of the Coating AlCrN for Special Applications. MATERIALS. 2021; 14. doi: 10.3390/ma14164651

[13] Nose M, Chiou WA, Kawabata T, Hatano Y, Matsuda K. Self-hardening effect of CrAlN/BN nanocomposite films deposited by direct current and radio frequency reactive cosputtering. Thin Solid Films. 2012; 523:6-10. doi: 10.1016/j.tsf.2012.05.063

[14] Gilewicz A, Jedrzejewski R, Myslinski P, Warcholinski B. Structure, Morphology, and Mechanical Properties of AlCrN Coatings Deposited by Cathodic Arc Evaporation. JOURNAL OF MATERIALS ENGINEERING AND PERFORMANCE. 2019; 28:1522-1531. doi: 10.1007/s11665-019-03934-2

[15] Chang YY, Chung CH, Tsai ZH, Tsai JM. Tribological and mechanical properties of AlCrBN hard coating deposited using cathodic arc evaporation. Surface and Coatings Technology. 2022; 432:128097. doi: 10.1016/j.surfcoat.2022.128097

[16] Cai F, Wang J, Zhou Q, Xue H, Zheng J, Wang Q, Kim KH. Microstructure evolution and high-temperature tribological behavior of AlCrBN coatings with various B contents. Surface and Coatings Technology. 2022; 430:127994. doi: 10.1016/j.surfcoat.2021.127994

[17] Tao L, Wang J, Fang W, Cai F, Xu D, Zhang S. Improved high temperature stability and enhanced high-speed dry cutting performance of AlCrBN coatings by alloying with B. International Journal of Refractory Metals and Hard Materials. 2025; 131:107206. doi: 10.1016/j.ijrmhm.2025.107206

[18] Wang Z, Wang Y, Li Z, Feng K, Huang J, Lu F, Yao C, Cai X, Wu Y. Investigation of C/Al-Cr-N multilayer coatings for stainless steel bipolar plate in polymer electrolyte membrane fuel cells. Surface and Coatings Technology. 2014; 258:1068-1074. doi: 10.1016/j.surfcoat.2014.07.028

[19] Jie S, An S, Pengjiao Z, Junzhou L. Microstructure, mechanical performance, thermal stability, and oxidation resistance of AlCrN/AlCrBN nano-multilayer coating. Surface and Coatings Technology. 2024; 493: 131301. doi: 10.1016/j.surfcoat.2024.131301

[20] Seidl WM, Bartosik M, Kolozsvári S, Bolvardi H, Mayrhofer PH. Mechanical properties and oxidation resistance of Al-Cr-N/Ti-Al-Ta-N multilayer coatings. Surface and Coatings Technology. 2018; 347:427-433. doi: 10.1016/j.surfcoat.2018.05.025

[21] Chang YY, Huang KC. Improvement of Tribological Performance of TiAlNbN Hard Coatings by Adding AlCrN. Materials. 2022; 15:7750. doi: 10.3390/ma15217750

[22] Xu YX, Chen L, Pei F, Du Y. Structure and thermal properties of TiAlN/CrN multilayered coatings with various modulation ratios. Surface and Coatings Technology. 2016; 304: 512-518. doi: 10.1016/j.surfcoat.2016.07.055

[23] Santoso RAB, Deendarlianto, Muflikhun MA. Tool wear and surface characteristics of TiAlN/AlCrN insert in high-speed turning of bimetal aluminium alloy-grey cast iron engine block. Materials Letters. 2025; 379:137714. doi: 10.1016/j.matlet.2024.137714

[24] Venkatesh R, Anbumalar, Rajakarunakaran S, Britto JJJ. Optimizing machining efficiency: a comprehensive study on PVD cathodic arc evaporation coated turning tool inserts with TiAlN/AlCrN multilayer coatings. MATERIALS RESEARCH EXPRESS. 2024; 11. doi: 10.1088/2053-1591/ad507e

[25] Vereschaka A, Grigoriev S, Tabakov V, Migranov M, Sitnikov N, Milovich F, Andreev N. Influence of the nanostructure of Ti-TiN-(Ti,Al,Cr)N multilayer composite coating on tribological properties and cutting tool life. Tribology International. 2020; 150:106388. doi: 10.1016/j.triboint.2020.106388

[26] Tritremmel C, Daniel R, Lechthaler M, Rudigier H, Polcik P, Mitterer C. Microstructure and mechanical properties of nanocrystalline Al-Cr-B-N thin films. Surface and Coatings Technology. 2012; 213:1-7. doi: 10.1016/j.surfcoat.2012.09.055

[27] Chen Z, Lou M, Geng D, Xu YX, Wang Q, Zheng J, Zhu R, Chen Y, Kim KH. Effect of the modulation geometry on mechanical and tribological properties of TiSiN/TiAlN nano-multilayer coatings. Surface and Coatings Technology. 2021; 423:127586. doi: 10.1016/j.surfcoat.2021.127586

[28] Chen J, Fang W, Gobinda G, Cai F, Tao L, Zhang S. Effects of multilayer structure on the high-speed dry-cutting performance of AlCrBN/AlCrN multilayer coatings. International Journal of Refractory Metals and Hard Materials. 2024; 121:106672. doi: 10.1016/j.ijrmhm.2024.106672

[29] Yuan Z, Han Y, Zang S, Chen J, He G, Chai Y, Yang Z, Fu Q. Analysis of the mechanical properties of TiN/Ti multilayer coatings using indentation under a broad load range. Ceramics International. 2021; 47: 10796-10808. doi: 10.1016/j.ceramint.2020.12.196

[30] Yang Y, Liao N, Zhang M, Li F. Evaluation of the elastic-plastic properties of SiCN coating system by finite element simulations. Journal of the European Ceramic Society. 2017; 37:3891-3897. doi: 10.1016/j.jeurceramsoc.2017.05.017

[31] Mareau C. A thermodynamically consistent formulation of the Johnson-Cook model. Mechanics of Materials. 2020; 143:103340. doi: 10.1016/j.mechmat.2020.103340

[32] Qi Y. Simulation and Experimental Study on theMeso-scale Cutting of Tungsten Carbide YG18. in, Nanjing University of Aeronautics and Astronautics, 2018.

[33] Klein CA. Anisotropy of Young's modulus and Poisson's ratio in diamond. Materials Research Bulletin. 1992; 27: 1407-1414. doi: 10.1016/0025-5408(92)90005-K

[34] Lukaszkowicz K, Sondor J, Paradecka A, Pawlyta M, Chmiela B, Pancielejko M, Szczucka-Lasota B, Wegrzyn T, Tanski T. Structure and Tribological Properties of AlCrN plus CrCN Coating. COATINGS. 2020; 10. doi: 10.3390/coatings10111084

[35] Xu JM, Zhang P, Ying PY, Pogrebnjak A, Ma CZ, Lin CH, Yang T, Wu JB, Wang TL, Grigoriev AY, Levchenko V. Thermal stability and mechanical properties of (Al,Cr,Ti,Si,Y)N multielement nitride coatings after annealing. JOURNAL OF MATERIALS RESEARCH AND TECHNOLOGY-JMR&T. 2025; 36:9619-9628. doi: 10.1016/j.jmrt.2025.05.210

[36] Galindo RE, Endrino JL, Martínez R, Albella JM. Improving the oxidation resistance of AlCrN coatings by tailoring chromium out-diffusion. Spectrochimica Acta Part B: Atomic Spectroscopy. 2010; 65:950-958. doi: 10.1016/j.sab.2010.09.005

[37] Chen TL, Hsu SY, Lai YT, Chang SY, Hung HH, Tsai SY, Duh JG. Influence of boron contents on mechanical properties and high-temperature tribological behavior in (AlCrNbTiB)N coatings. JOURNAL OF VACUUM SCIENCE & TECHNOLOGY A. 2023; 41. doi: 10.1116/6.0002538

[38] Hu C, Chen L, Moraes V. Structure, mechanical properties, thermal stability and oxidation resistance of arc evaporated CrAlBN coatings. Surface and Coatings Technology. 2021; 417:127191. doi: 10.1016/j.surfcoat.2021.127191

[39] Fuentes GG, Pérez-Gandarilla L, Medrano A, Fernández Palacio J, Bueno R, Arias-Egido E, Fernández J. Microstructure and indentation hardness study of CAE-PVD (Cr,Ti,Al)N solid solution coatings deposited using a combinatorial multitarget approach. Surface and Coatings Technology. 2021; 420:127326. doi: 10.1016/j.surfcoat.2021.127326

[40] Sattari-Esfahlan SM, Mirzaei S, Josline MJ, Moon JY, Hyun SH, Jang H, Lee JH. Amorphous boron nitride: synthesis, properties and device application. NANO CONVERGENCE. 2025; 12. doi: 10.1186/s40580-025-00486-1

[41] Gao Y, Cai F, Lu X, Xu W, Zhang C, Zhang J, Qu X. Design of cycle structure on microstructure, mechanical properties and tribology behavior of AlCrN/AlCrSiN coatings. Ceramics International. 2022; 48: 12255-12270. doi: 10.1016/j.ceramint.2022.01.087

[42] Fang W, Chen J, Cai F, Zhou Q, Li M, Zhang S. Reduced crater wear and improved high-speed dry cutting performance of B-containing AlTiBN coatings against Ti-6Al-4 V alloy. Tribology International. 2023; 187:108730. doi: 10.1016/j.triboint.2023.108730

[43] Xu YX, Chen L, Pei F, Du Y. Structure and thermal properties of TiAlN/CrN multilayered coatings with various modulation ratios. SURFACE & COATINGS TECHNOLOGY. 2016; 304:512-518. doi: 10.1016/j.surfcoat.2016.07.055

[44] Usman M, Zhou Z, Zia AW, Li KY. Designing hydrogen-free diamond like multilayer carbon coatings for superior mechanical and tribological performance. Tribology International. 2024; 192:109211. doi: 10.1016/j.triboint.2023.109211

[45] Leyland A, Matthews A. On the significance of the H/E ratio in wear control: a nanocomposite coating approach to optimised tribological behaviour. Wear. 2000; 246:1-11. doi: 10.1016/S0043-1648(00)00488-9

[46] Wang T, Wu Y, Qi Z, Zhao Y, Zhang J, Zhan L, Yin L. Stress Analysis of Multilayered Coatings Subjected to Surface Point Contact Loading Based on Its Three-Dimensional Elastic Field Solution. in: Coatings, 2020, pp. 838. doi: 10.3390/coatings10090838

[47] Han X, Shao Y, Ji H, Zhao Q, Wang Y, Zhang X. Interfacial stress and failure behavior of EB-PVD YSZ thermal barrier coatings with different bond coats. Surfaces and Interfaces. 2026; 87:108889. doi: 10.1016/j.surfin.2026.108889